Projected Tasman Sea Extremes in Sea Surface Temperature through the Twenty-First Century

ERIC C. J. OLIVER

Institute for Marine and Antarctic Studies, University of Tasmania, and Australian Research Council Centre of Excellence for Climate System Science, Hobart, Tasmania, Australia

SIMON J. WOTHERSPOON

Institute for Marine and Antarctic Studies, University of Tasmania, Hobart, Tasmania, Australia

MATTHEW A. CHAMBERLAIN

CSIRO Marine and Atmospheric Research, Hobart, Tasmania, Australia

NEIL J. HOLBROOK

Institute for Marine and Antarctic Studies, University of Tasmania, and Australian Research Council Centre of Excellence for Climate System Science, Hobart, Tasmania, Australia

(Manuscript received 29 April 2013, in final form 14 November 2013)

ABSTRACT

Ocean climate extremes have received little treatment in the literature, aside from coastal sea level and temperatures affecting coral bleaching. Further, it is notable that extremes (e.g., temperature and precipitation) are typically not well represented in global climate models. Here, the authors improve dynamically downscaled ocean climate model estimates of sea surface temperature (SST) extremes in the Tasman Sea off southeastern Australia using satellite remotely sensed observed extreme SSTs and the simulated marine climate of the 1990s. This is achieved using a Bayesian hierarchical model in which the parameters of an extreme value distribution are modeled by linear regression onto the key marine climate variables (e.g., mean SST, SST variance, etc.). The authors then apply this fitted model, essentially a form of bias correction, to the marine climate projections for the 2060s under an A1B emissions scenario. They show that the extreme SSTs are projected to increase in the Tasman Sea in a nonuniform way. The 50-yr return period extreme SSTs are projected to increase by up to 2°C over the entire domain and by up to 4°C in a hotspot located in the central western portion of the Tasman Sea, centered at a latitude ~500 km farther south than the projected change in mean SST. The authors show that there is a greater than 50% chance that annual maximum SSTs will increase by at least 2°C in this hotspot and that this change is significantly different than that which might be expected because of random chance in an unchanged climate.

1. Introduction

Understanding the behavior of extreme events in the ocean, particularly in a changing climate, is important for many aspects of the marine climate system. The behavior of extremes helps us understand the relationship between extreme events and the underlying marine climate (e.g., mean, variances, etc.) and can lead to a better understanding of the physical mechanisms that underpin the dynamics of extreme events. Extreme events also play an important role in the distribution of ecological habitats and species. Marine species can typically survive over a finite range of environmental conditions (e.g., ocean temperatures). Abrupt changes to these conditions, which may be associated with a rapidly changing climate and/or a tipping point, can perturb the system in a way that is potentially hazardous or even catastrophic for the habitat or species. In 2011, for example, a ''marine heat wave'' was recorded off Western Australia (Pearce

Corresponding author address: Eric C. J. Oliver, Institute for Marine and Antarctic Studies, Private Bag 129, University of Tasmania, Hobart, TAS 7001, Australia.
E-mail: eric.oliver@utas.edu.au

DOI: 10.1175/JCLI-D-13-00259.1

and Feng 2012) causing shifts in habitat distributions of various species, including seaweeds, invertebrates, and fish, which not only occurred during the event but persisted after the event had dissipated (Wernberg et al. 2012).

The study of extreme events in the environment extends back at least to the origins of the extremes field with Emil Gumbel and his examination of hydrological extremes: for example, floods (Gumbel 1941, 1958). Additionally, several important advances in extreme value theory owe their origins to researchers studying hydrological extremes: for example, the ''peak over threshold'' approach (Shane and Lynn 1964; Todorovic and Zelenhasic 1970). The study of extremes in the atmosphere is also well developed, with particular areas of focus including rainfall (e.g., Coles and Tawn 1996; Cooley et al. 2007), air temperatures (e.g., Mearns et al. 1984; Alexander et al. 2006), and wind speeds (e.g., Hennessey 1977; Cook 1985; Zwiers 1987; Coles and Walshaw 1994). Extreme value analysis has also been applied directly to global climate model output to assess the projected changes in extreme events under climate change scenarios (McGuffie et al. 1999; Kharin et al. 2007; Perkins et al. 2013).

Clearly, extreme events have been well studied in hydrology and in the atmospheric sciences, but oceanic extremes have received relatively little attention. The close relationship between sea level variability and hydrology, as well as the availability of long (multidecadal) high-resolution (hourly) sea level records, has meant that much of the examination of oceanic extremes has focused on sea level (e.g., Pugh and Vassie 1980; Tawn and Vassie 1989; Tawn 1992; Dixon et al. 1998; Church et al. 2006; Bernier and Thompson 2006; Hunter 2010). The study of extreme ocean currents and technical issues related to the bivariate nature of this variable also date back several decades (Pugh 1982; Carter et al. 1987; Griffiths 1996; Oliver et al. 2012), and there has been some attention paid to extreme ocean wave heights (Muir and El-Shaarawi 1986; Dawson 2000; Caires and Sterl 2005). However, the study of ocean temperature and salinity is relatively new and few oceanographers are familiar with the techniques of extreme value theory. In this study, we will examine extreme sea surface temperatures (SSTs). To our knowledge, no previous large-scale ocean climate studies have focused on understanding the nature of marine climate extremes from an extreme value perspective.

Oceanic and atmospheric circulation models—and, by extension, climate models—generally have a poor representation of extreme events. This is often related to the relationship between extreme events and physical processes, which operate on scales smaller than the model can resolve. For example, the representation of precipitation extremes in climate models is poor—models often drizzle over large areas and fail to simulate the frequency and magnitude of heavy rainfall events (e.g., Perkins et al. 2007)—while their representation of air temperature extremes is regarded as acceptable (Randall et al. 2007). The representation of tropical cyclones is often poor, in terms of frequency and intensity, and is sensitive to the choice of convective parameterization (Randall et al. 2007). For the ocean, the resolution of ocean general circulation models is often too coarse to resolve mesoscale eddies, which is a large source of internal oceanic variability. Furthermore, ocean surface fluxes are usually specified either from atmospheric model output or by two-way coupling with an atmospheric model, and therefore these forcing fields suffer from the same underrepresentation of extremes as the atmospheric models themselves. Hence, even if the ocean models can resolve the extremes due to internal variability, their forcing fields often do not contain the relevant or appropriate representation of atmospheric extremes.

Nevertheless, circulation models do simulate the overall climate well. Here, we define climate as the ''central statistics'' (e.g., mean, variance, etc.) of the environmental variables (e.g., temperature, circulation, etc.) and will use those terms interchangeably. In the context of climate extremes we are often concerned with relatively common extremes (e.g., heat waves, the upper 95th percentile) and thus not necessarily the far tails of the probability distribution. The tails of common probability distributions can be related to the central moments (e.g., Berman 1964) and we can see this intuitively for events that are not too extreme. For example, if the mean or the variance increases, so too should the extremes, and higher-order central moments such as the skewness and kurtosis can be anticipated to have predictable consequences on the shape of the distribution's tails. Previous studies have shown that air temperature extremes can be estimated using the central moments such as the mean temperature (Griffiths et al. 2005) or a combination of the mean, variance, and skewness (Ballester et al. 2010). In addition, Simolo et al. (2011) modeled extreme temperatures using the first four L moments and de Vries et al. (2012) estimated changes in extremes between the present and a possible future climate using the mean and variance alone. Our aim is to develop an extremes model that is able to recover the observed extremes and estimate future extremes given projections of ocean climate over the observed and future time periods.

This paper is organized as follows: The marine climate, simulated by an eddy-resolving ocean model, is presented and evaluated against the observed marine climate in section 2. A review of extreme value theory is

presented in section 3 followed by its application to the observed and simulated 1990s SST extremes off southeastern Australia. An improved estimation of the simulated extreme events, for both the 1990s and the 2060s, is presented in section 4 using a Bayesian hierarchical model and the marine climate as predictors of the extremes. A summary and discussion are presented in section 5.

2. Observed and model simulated marine climate

The ocean model output and observations are described in sections 2a and 2b, respectively, followed by an evaluation of the modeled marine climate in section 2c.

a. *Ocean model simulations of the 1990s and the 2060s*

The Ocean Forecasting Australia Model (OFAM; Oke et al. 2008) was used to model the marine climate off of southeastern Australia. The model has near-global coverage (70°S–70°N) with 47 z levels in the vertical (10-m resolution in the upper 200 m). The horizontal resolution is 1/10° in latitude and longitude (eddy resolving) in the Australasia region (90°E–180°, 70°S–20°N) but coarsening outside of this domain up to 2° in latitude and longitude in the North Atlantic Ocean. OFAM underpins the Bluelink ocean forecasting and the Bluelink Reanalysis (BRAN) systems developed by the Centre for Australian Weather and Climate Research.

In the present study, we examine dynamically downscaled climate projections using OFAM, forced by a reanalysis representation of the historical (1990s) climate and by global climate model projections of climate change, for the decades of the 1990s and 2060s. The downscaled projection of the 2060s was forced with a climatology of 2060s fluxes, based on output from the GCM climate run, in order to reduce the influence of low-frequency climate variations on the results. A control experiment (CTRL) with a climatology built from observed 1990s fluxes was run for comparison with the projection. Estimations of marine climate from the CTRL run were evaluated against the observations in section 2c.

The dynamical downscaling simulations of climate change projections are described elsewhere (Chamberlain et al. 2012; Sun et al. 2012) and the details are summarized here. Fields of "normal year" ocean surface fluxes of heat, freshwater and momentum were generated from 40-yr European Centre for Medium-Range Weather Forecasts (ECMWF) Re-Analysis (ERA-40) output (Uppala et al. 2005) for the decade of the 1990s. This normal-year forcing represents typical atmospheric variability on all time scales shorter than 1 yr, but major climate indices such as El Niño, Indian Ocean dipole, etc., are in neutral states. In CTRL, OFAM was forced repeatedly by this normal-year forcing. Repeat annual forcings were used because of the difficulty in running the high-resolution model long enough to faithfully reproduce the low-frequency variability, which is important to the distribution of extreme events. Hence, this variability was deliberately removed from the experiments. Global climate model [Commonwealth Scientific and Industrial Research Organisation Mark, version 3.5 (CSIRO Mk3.5)] simulations, forced under the A1B emissions scenario, provide climate change projections through the twenty-first century. In what we refer to as the A1B experiment, the CSIRO Mk3.5 projected change was added to the normal-year forcing and was used to force OFAM.

We obtain daily mean sea surface temperature T, sea surface height η, and surface horizontal currents $\mathbf{u}$ from the last 9 yr for both simulations. Sample time series of T at four locations in the Tasman Sea are shown in Fig. 1. Because of our regional ecological interests in a broader funded project, we restrict our domain to be bounded by 144°E, 169°E, 48°S, and 20°S and ignore all grid cells with water depth less than 200 m. This latter constraint eliminates from the analysis all model estimates on the continental shelf, where OFAM has much less skill (Oliver and Holbrook 2014). A set of marine climate statistics was calculated for each simulation and these statistics are listed in Table 1. Each statistic is a vector of length J, where J is the total number of grid cells in latitude and longitude. Additionally, the annual maxima of T were calculated at all locations and denoted $\hat{\mathbf{Y}}$ where $\hat{\mathbf{Y}} = \{\hat{\mathbf{y}}_j \,|\, j = 1, 2, \ldots, J\}$ is a list of vectors, with $\hat{\mathbf{y}}_j$ being a vector of length 9, representing the nine annual maxima at the jth location. For computational efficiency, only every fifth grid cell in latitude and longitude was retained.

b. *Ocean observations*

Daily fields of observed SSTs from the Advanced Very High Resolution Radiometer (AVHRR) were obtained from the Jet Propulsion Laboratory (http://podaac.jpl.nasa.gov/) for the period 1 January 1982–31 December 2009 (28 yr) and are defined on a 4-km grid. It was desirable to regrid these AVHRR data onto the same grid as the OFAM output. Thus, for each OFAM grid location, the nearest AVHRR grid point was first identified and then a spatial average of SST was calculated from the mean of nine locations in a 3×3 box centered on this location. This spatial average was performed to partially compensate for the many missing values (up to 90% at some locations) present in the daily 4-km-resolution AVHRR data. The linear trend was then removed by linear regression from the time series at each location independently, and the mean, variance,

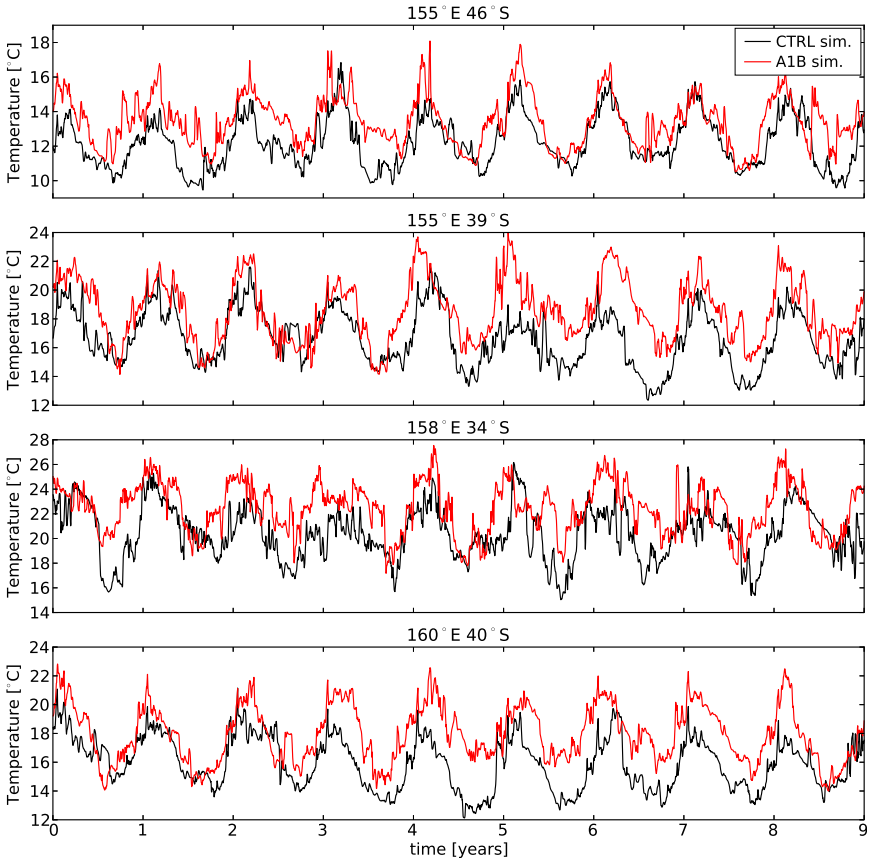

FIG. 1. Time series of simulated SST. The SST time series at four locations are shown for the 1990s (the CTRL simulation; black lines) and the 2060s (the A1B simulation; red lines). Locations are shown in Fig. 2 (top right).

and third central moment were calculated along with the 28 annual maxima at all locations $\mathbf{Y} = \{\mathbf{y}_j \,|\, j = 1, 2, \ldots, J\}$.

Weekly fields of isostatically adjusted sea level on a ¼° grid were obtained from Archiving, Validation, and Interpretation of Satellite Oceanographic data (AVISO; http://www.aviso.oceanobs.com/) for the period 14 October 1992–22 July 2009. The variance of sea level was calculated at each location in space. Global mean dynamic topography (MDT), which is mainly caused by the average large-scale circulation patterns such as the East Australian Current (EAC) in the Tasman Sea region, was obtained from the National Space Institute, Technical University of Denmark (Andersen and Knudsen 2009). We used the DTU10 product, which is defined on a horizontal grid with 1-min resolution in latitude and longitude.

c. *Evaluation of model simulated marine climate*

The 1990s marine climate estimated by the CTRL simulation has been evaluated here against observed marine climate statistics. The simulated marine climate fields have been smoothed with an isotropic Gaussian filter to remove all variability with wavelengths of 2.5° or less in latitude and longitude.

A comparison of observed and simulated mean SST $\boldsymbol{\mu}$, SST variance $\boldsymbol{\sigma}^2$, and SST third central moment $\mathbf{m}_3$ can be seen in Fig. 2. The mean SST is very well represented by the model, showing a strong meridional

TABLE 1. List of marine climate statistics calculated from ocean model simulations. A dash in the last column indicates a unitless statistic.

Name	Variable	Units
T mean (first central moment)	$\boldsymbol{\mu}$	°C
T variance (second central moment)	$\boldsymbol{\sigma}^2$	°C^2
T third central moment	$\mathbf{m}_3$	°C^3
T fourth central moment	$\mathbf{m}_4$	°C^4
T skewness ($\mathbf{m}_3/\boldsymbol{\sigma}^{3/2}$)	$\boldsymbol{\gamma}$	—
T excess kurtosis ($\mathbf{m}_4/\boldsymbol{\sigma}^4 - 3$)	$\boldsymbol{\kappa}$	—
η variance	$\boldsymbol{\sigma}_\eta^2$	m^2
Eddy kinetic energy (per unit mass and volume)	$\mathbf{K}$	m^2 s^{-2}

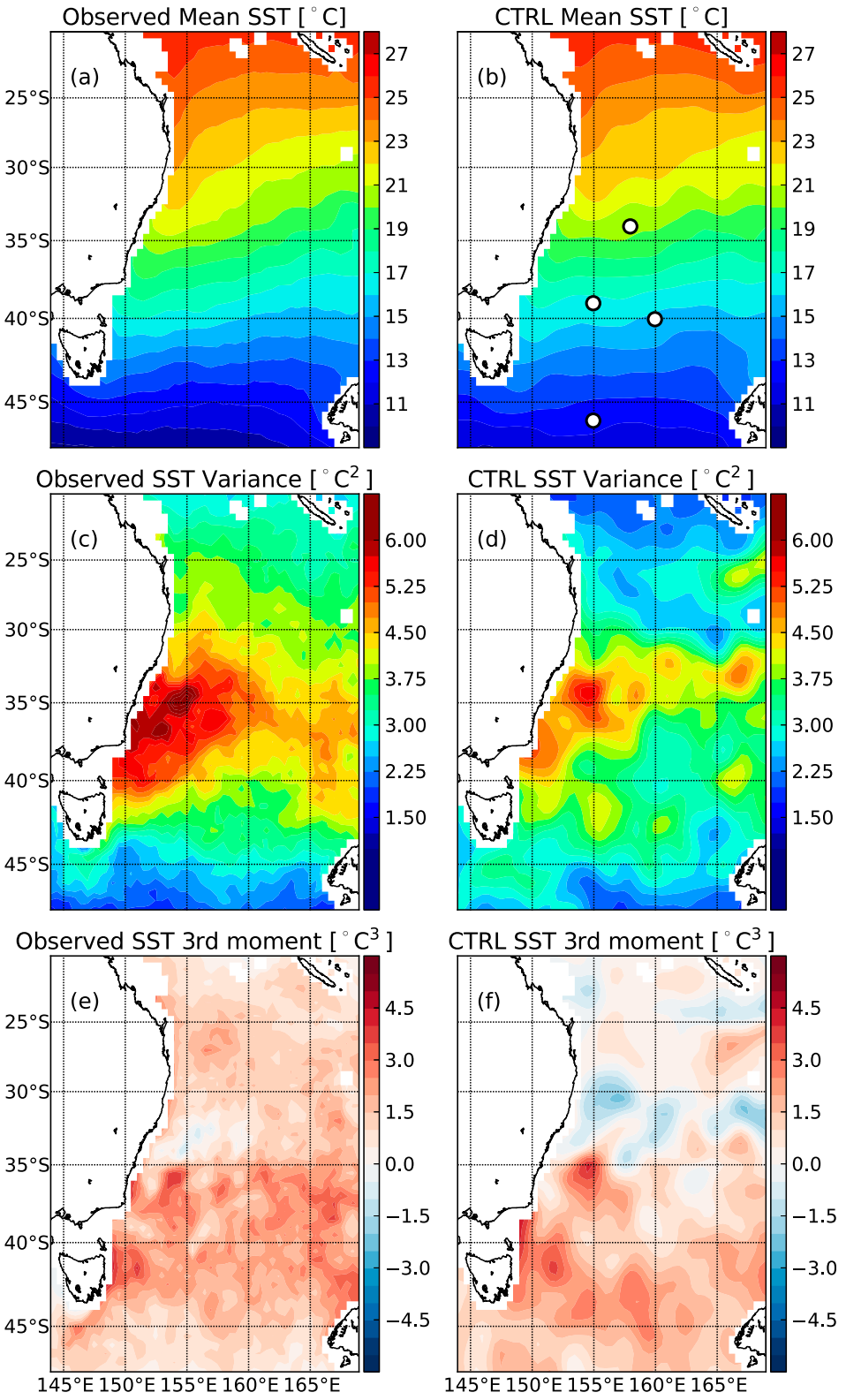

FIG. 2. Comparison of observed and simulated SST climate statistics: (top) mean SST, (middle) SST variance, and (bottom) the SST third central moment for (left) the observations and (right) the CTRL simulation.

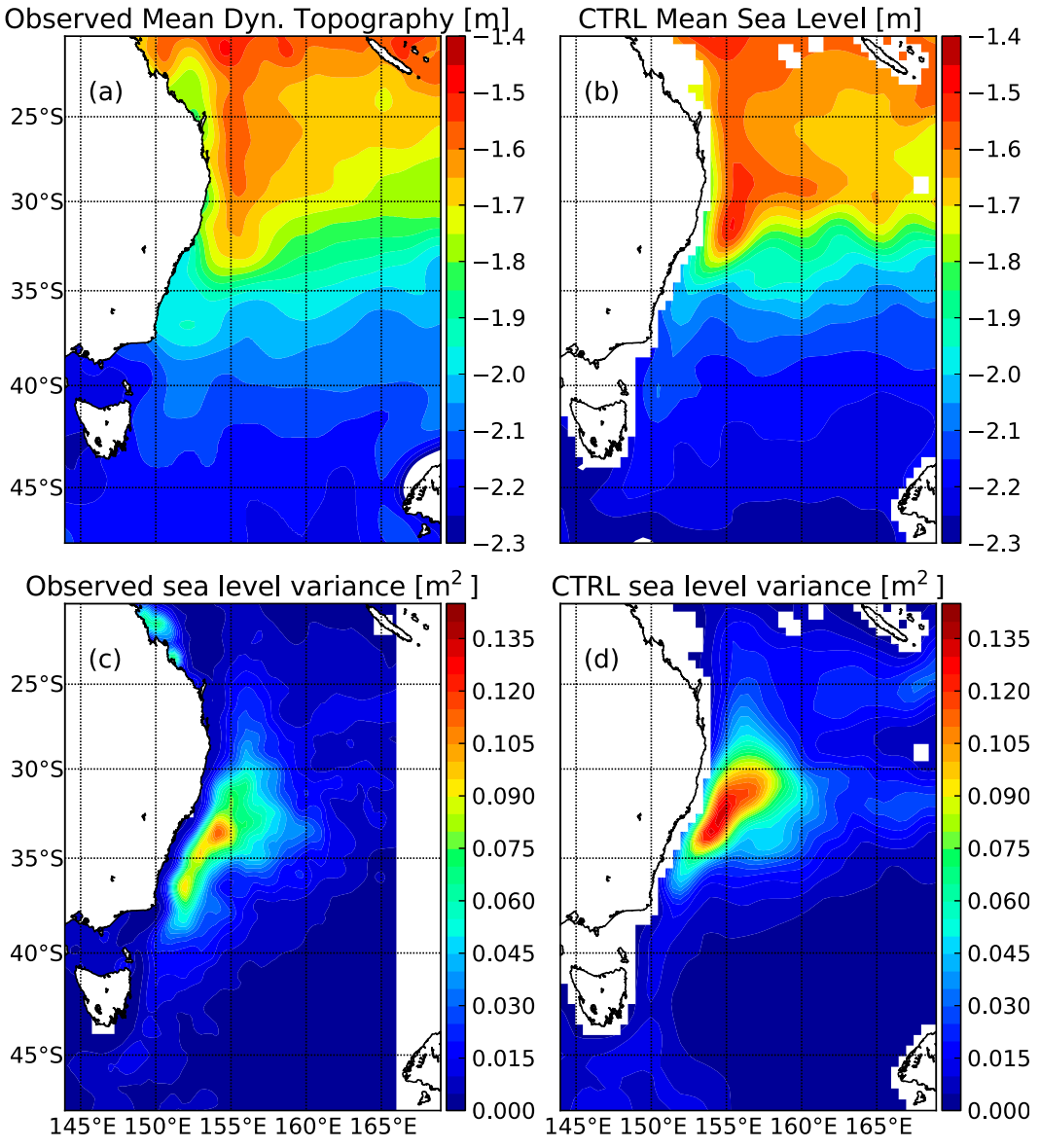

FIG. 3. Comparison of observed and modeled sea level. (a) The observed mean dynamic topography and (b) the CTRL simulation mean sea levels (b). (c) The observed and (d) CTRL simulation sea level variances.

gradient of SST ranging from 10°–11°C in the south to 26°–27°C in the north and a zonal gradient in SST near the Australian continent associated with the southward-flowing EAC (Figs. 2a,b). The mean is slightly overestimated (~1°C) in the extreme south. The SST variance is also well represented showing a region of high variance bounded by the Australian landmass and lying between 32° and 43°S (Figs. 2c,d). This region roughly corresponds to the separation point of the East Australian Current (~33°S) and its eddy-rich southward extension (Godfrey et al. 1980; Stammer 1997; Suthers et al. 2011; Brassington et al. 2011). The SST variance in the CTRL simulation is lower in magnitude and less smooth in space, most likely at least partly due to the shorter time over which the statistics are calculated (9 yr for the simulations and 28 yr for the observations). The SST third central moment is also reasonably well represented with positive values in the Tasman Sea south of the EAC separation point, due to a large proportion of eddies being anticyclonic and thus warm-core eddies (e.g., Thompson and Demirov 2006), and negative values immediately to the north (Figs. 2e,f). The positive values in the tropical region are not well represented.

The simulated mean sea level compares well against the observed mean dynamic topography (Figs. 3a,b; MDT has been shifted by −2.7 m to facilitate comparison with mean

sea level). Regions of strong gradients clearly show the EAC along the east coast of Australia and its separation, as well as subsequent eastward flow, around 33°S. A continuation of this pattern southward to Tasmania indicates the presence of the EAC extension (Stammer 1997; Brassington et al. 2011). Note that, because of the technique used to calculate the mean dynamic topography, specifically the use of gravity-based measurements of the geoid, it will appear artificially smooth in comparison to the simulated mean sea level (Andersen and Knudsen 2009). Finally, sea level variance is well represented by the CTRL simulation (Figs. 3c,d). The eddy-rich EAC separation and extension regions appear in both the observed and simulated fields. The simulations slightly overestimate the sea level variance (by 0.01–0.02 m^2) and place the region of largest variance farther north (1°–2° of latitude) than in the observations. The velocities, transport, and seasonal cycle of the ocean model representation of the EAC have been evaluated against observations in more detail by Sun et al. (2012); the simulated eddy-rich EAC extension, which extends south from the separation point, has been discussed by Matear et al. (2013).

3. Observed and model simulated extreme SSTs

Extreme value theory is outlined in section 3a followed by its direct application to observed and simulated SST annual maxima in section 3b.

a. Extreme value theory

There are two common ways to model extreme values. The ''block maxima'' approach fits the generalized extreme value (GEV) distribution to a collection of data maxima taken over subsets of the data (e.g., monthly maxima, annual maxima, etc.). The peak-over-threshold approach fits the generalized Pareto distribution to data values greater than a predefined threshold (e.g., the 95th percentile). In both cases, the fitted distribution can be used to estimate extreme values with return periods longer than the original record length. For our purposes, the block-maxima approach is preferred since (i) we have a natural block size, due to seasonal variability, over which to calculate maxima (i.e., 1 yr) and (ii) the peak-over-threshold approach would require a separate model for the threshold parameter when we later apply the Bayesian hierarchical approach discussed in section 4.

A general overview of extreme value theory and practical aspects of its application can be found in Coles (2001). Here, we summarize those aspects relevant for the present study. Consider a stationary sequence of random variables $\{x_t \,|\, t = 1, 2, \ldots\}$. Let y denote the maximum of x_t over a block of length n,

$$y = \max(x_1, x_2, \ldots, x_n). \tag{1}$$

In the limit $n \to \infty$, the distribution function of y converges to one of three types, which can be summarized by the GEV distribution,

$$F_{\mathrm{GEV}}(y \,|\, a, b, \xi) = \exp\left\{-\left[1 + \xi\left(\frac{y-a}{b}\right)\right]^{-1/\xi}\right\}, \tag{2}$$

where a is the location parameter, $b > 0$ is the scale parameter, and ξ is the shape parameter. For $\xi \to 0$ the GEV converges to the Gumbel (type I) distribution, for $\xi > 0$ it converges to the Fréchet (type II) distribution, and for $\xi < 0$ it converges to the Weibull (type III) distribution.

The relatively short record length (28 yr for observed SSTs and 9 yr for the model simulations) could lead to unstable estimates of the shape parameter. This instability could be especially problematic when developing a model for the extreme value distribution parameters where stationarity is assumed across the decades of the 1990s and 2060s. Therefore, we elect to use the Gumbel (type I) distribution, which is given by

$$F_{\mathrm{I}}(y \,|\, a, b) = \exp\left[-\exp\left(-\frac{y-a}{b}\right)\right] \tag{3}$$

and has dependence only on the location parameter a and the scale parameter b.

The return level z_L for a return period L is related to the quantiles of the Gumbel distribution by

$$z_L(y) = a - b\log[-\log F_{\mathrm{I}}(y \,|\, a, b)] \tag{4}$$

and the quantiles of the Gumbel distribution are in turn related to the return period by

$$L(y) = [1 - F_{\mathrm{I}}(y \,|\, a, b)]^{-1}, \tag{5}$$

where the units of z_L are the same as the units of y and the units of L are given by the block length used in Eq. (1): for example, if the block length is 1 yr, then L has units of years. For a fitted Gumbel distribution, one can estimate z_L given a return period L and vice versa using Eqs. (4) and (5).

b. Estimates of extreme SSTs

The Gumbel distribution was fitted to the observed and CTRL simulation annual maxima using maximum likelihood, providing estimates of the Gumbel distribution parameters. From the estimated values and the theory outlined above, it is possible to estimate the return level for return periods longer than the original record length. We choose the return level $\mathbf{z}_{50}$, corresponding to

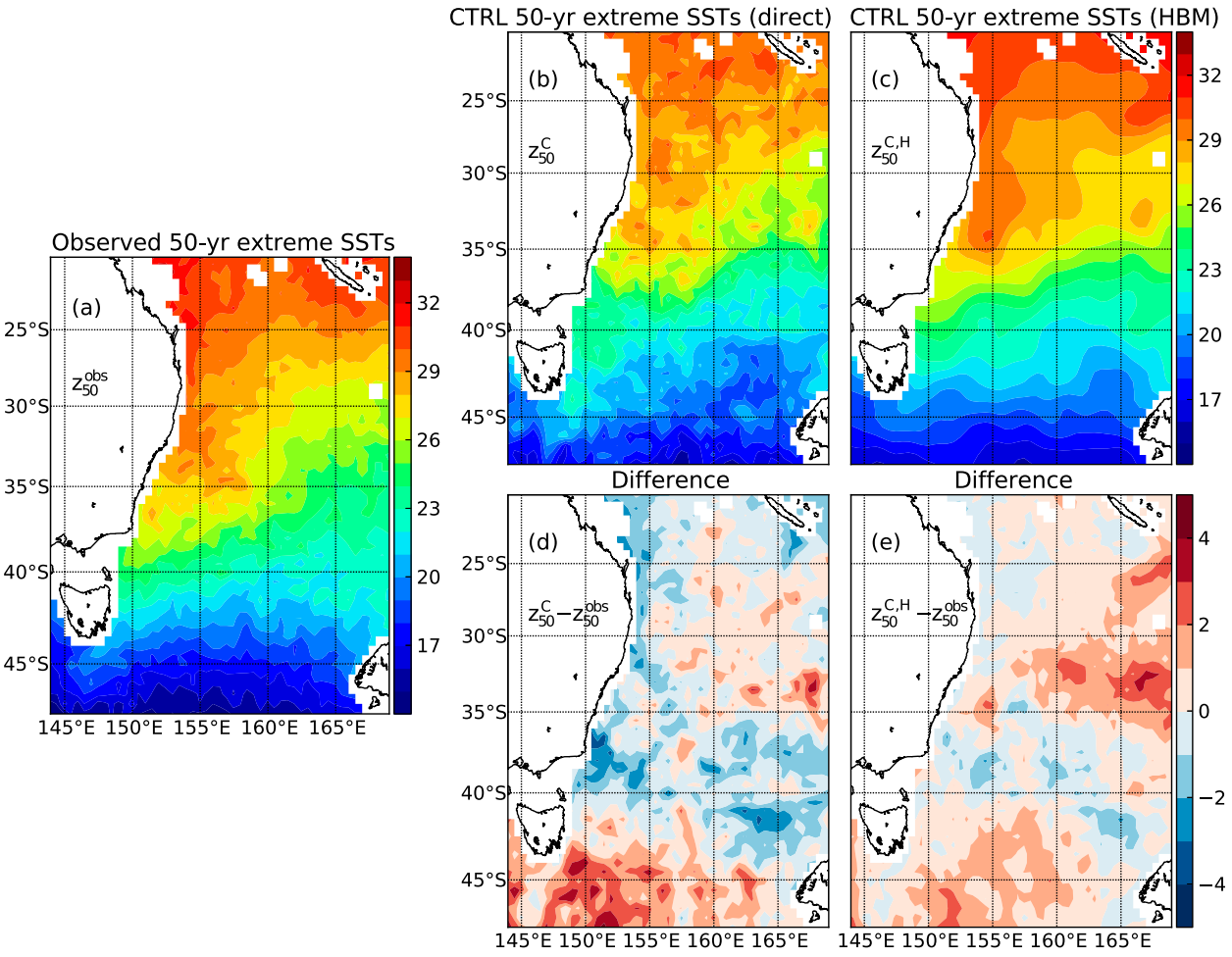

FIG. 4. The 50-yr return levels for observed and CTRL simulation sea surface temperatures. The 50-yr return levels were estimated for (a) the observations and (b) the CTRL simulation, using maximum likelihood fits of the Gumbel distribution to the annual maxima and (c) for the CTRL simulation using the Bayesian hierarchical model (see section 4b for description of selected model). (d),(e) The difference between the two estimates of the CTRL simulation extremes and the observations are shown.

a return period of 50 yr, to represent a suitably extreme event. We also tried a return period of 20 yr and found that the results were not sensitive to this choice.

The $\mathbf{z}_{50}$, derived from observed SSTs and denoted $\mathbf{z}_{50}^{\text{obs}}$, is dominated by the mean SST (Fig. 4a). There is a strong meridional gradient in $\mathbf{z}_{50}^{\text{obs}}$ ranging from approximately 14°C in the south (at ~50°S) to 32°C in the northern Coral Sea (at ~20°S). It is interesting to note that over a large proportion of the domain the contours of $\mathbf{z}_{50}^{\text{obs}}$ run roughly east–west, as do contours of mean SST (see Fig. 2a): that is, there is a strong zonality in both the extremes and the background mean SST. However, north of 38°S and west of 162°E (the eddy-rich EAC separation zone) these contours deviate strongly from this zonality and reflect more the mean position of the EAC separation and the large SST variance found there (see Fig. 2c). Therefore, it appears that both the mean SST and the SST variance play a strong role in the spatial distribution of extreme SSTs.

The $\mathbf{z}_{50}$, derived from the CTRL simulation and denoted $\mathbf{z}_{50}^{C}$, exhibit a similar pattern as $\mathbf{z}_{50}^{\text{obs}}$ (Fig. 4b). The strong meridional gradient is present although the extremes are overpredicted by up to 4°C in a broad region southeast of Tasmania (see Fig. 4d for a map of $\mathbf{z}_{50}^{C} - \mathbf{z}_{50}^{\text{obs}}$). The tilting of contours in the EAC separation zone is present but less clearly defined than in the observations. Additionally, $\mathbf{z}_{50}^{C}$ exhibits a lot of high wavenumber variability that is not present in the observations, and this is clearly reflected in the difference map.

The differences between $\mathbf{z}_{50}^{C}$ and $\mathbf{z}_{50}^{\text{obs}}$ are generally less than ±3°C over most of the domain. However, isolated residual differences exceed ±3°C and even ±4°C in subregions southeast of Tasmania, off the southeast cost of mainland Australia, northwest of New Zealand's South

Island, and in the central eastern portion of the domain. While these differences may be smaller than expected given the model resolution and the nature of the GCM-derived forcing fields, we demonstrate in the next section that it is possible to improve upon these estimates using more sophisticated extreme value techniques applied to the model output.

4. Improving model simulated extreme SSTs

In this section, we develop an extreme value model (sections 4a and 4b) and show that it provides improved estimates of the SST extremes using output from the CTRL simulation, when evaluated against observations (section 4c). Following this evaluation, we apply the model to the A1B simulation output (section 4d) and discuss the role played by individual marine climate variables in the estimated change of extreme SSTs (section 4e).

a. Modeling extremes using climate statistics

The CTRL simulation provides good estimates of the large-scale circulation and the marine climate (section 2c). However, we believe the estimates of SST extremes can be improved (section 3b). Inspired by previous studies of extremes (e.g., Griffiths et al. 2005; Ballester et al. 2010; Simolo et al. 2011; de Vries et al. 2012), we develop a simple approach of modeling extreme SSTs using the basic marine climate statistics from the model simulation output.

The modeling of SST extremes as a function of marine climate variables is performed here using a Bayesian hierarchical model (BHM; e.g., Cooley et al. 2007; Cressie and Wikle 2011). The observed SST annual maxima $\mathbf{Y}$ are modeled using a Gumbel distribution, as in section 2. However, we now model the parameters of the Gumbel distribution as a function of a latent spatial process. This latent spatial process is characterized by the marine climate: for example, the mean SST, SST variance, and so on. This model is based on the fundamental assumption that there exists an important physical connection (relationship) between the underlying climate of the marine system and the behavior of its extremes. The assumption that the model characterizes a physical relationship that is invariant in time and space, rather than a purely probabilistic relationship, allows us to assume stationarity in the model parameters and use the fitted model to estimate extremes in a projected climate.

The latent spatial process is modeled here as a linear regression of the Gumbel distribution parameters onto the marine climate,

$$\mathbf{a} = \mathbf{X}\boldsymbol{\beta}_a + \epsilon_a \quad \text{and} \tag{6}$$

$$\phi = \mathbf{X}\boldsymbol{\beta}_\phi + \epsilon_\phi, \tag{7}$$

where $\mathbf{X}$ is a $J \times M$ design matrix constructed from the marine climate variables (the covariates), $\boldsymbol{\beta}_a$ and $\boldsymbol{\beta}_\phi$ are vectors (of length M) of regression coefficients, and ϵ_a and ϵ_ϕ are vectors (of length J) of error terms characterizing effects not included in the model. Here, M is the number of covariates included in the model plus one (the plus one indicates the required column of ones in $\mathbf{X}$) and J is the number of spatial locations considered. The error terms ϵ_a and ϵ_ϕ are normally distributed with zero mean and covariance matrices $\tau_a^{-1}\mathbf{I}$ and $\tau_\phi^{-1}\mathbf{I}$, respectively, where $\mathbf{I}$ is the identity matrix and τ_a and τ_ϕ are error precisions.[1] The Gumbel distribution parameters at all locations J have been combined into the vectors $\mathbf{a}$ and $\mathbf{b}$; since the scale parameter $\mathbf{b}$ is constrained to be positive, it has been rescaled as $\phi = \log\mathbf{b}$ to allow ϕ to take on both positive and negative values. The model is described in more detail, including technical aspects of the Bayesian approach, in appendix A and in the more detailed companion paper by Oliver et al. (2014, hereafter OWH).

The marine climate statistics are first collected together into the covariate matrix $\mathbf{X}$. This matrix may include of any subset of the possible covariates listed in Table 1. For example, if we include the mean SST $\boldsymbol{\mu}$, SST variance $\boldsymbol{\sigma}^2$, and the eddy kinetic energy $\mathbf{K}$, the design matrix is written as

$$\mathbf{X} = [\mathbf{1} \,|\, \boldsymbol{\mu} \,|\, \boldsymbol{\sigma}^2 | \mathbf{K}], \tag{8}$$

where $\mathbf{1}$ is a vector of ones, and the linear regression equations for $\mathbf{a}$ and ϕ become

$$\mathbf{a} = \beta_{a,0} + \beta_{a,1}\boldsymbol{\mu} + \beta_{a,2}\boldsymbol{\sigma}^2 + \beta_{a,3}\mathbf{K} + \epsilon_a \quad \text{and} \tag{9}$$

$$\phi = \beta_{\phi,0} + \beta_{\phi,1}\boldsymbol{\mu} + \beta_{\phi,2}\boldsymbol{\sigma}^2 + \beta_{\phi,3}\mathbf{K} + \epsilon_\phi. \tag{10}$$

It is possible to include different sets of covariates separately into the two regression models, but for simplicity we choose the same set of covariates for both models. Note that the regression coefficients and the error terms do not vary in space. They express an underlying connection between the climate statistics and the Gumbel distribution parameters that is taken to hold at every location in space.

We sample for the regression coefficients and error variances using a Markov chain Monte Carlo (MCMC) technique (e.g., Spiegelhalter et al. 2002). Within each step of the MCMC loop, we draw samples of $\mathbf{a}$ and ϕ and

[1] We are using the convention, common in the Bayesian approach, of expressing variance σ^2 as the reciprocal of the precision τ^{-1} (e.g., Gelman et al. 2003).

TABLE 2. Comparison of candidate models. The covariates included in the model are listed in the first column. The other columns indicate measures of model fit ($\overline{D}$) and model complexity (pD) as well as the deviance information criteria and Bayesian predictive information criteria scores. The DIC and BPIC scores in bold indicate the preferred models at each stepwise regression step; the DIC and BPIC scores in bolded italics indicate the preferred model overall.

Covariates included in model	$\overline{D}$	pD	DIC	BPIC
$\boldsymbol{\mu}$	165 257	4608	**169 865**	**174 473**
$\boldsymbol{\mu}$, $\boldsymbol{\sigma}^2$	154 443	4655	**159 098**	**163 753**
$\boldsymbol{\mu}$, $\mathbf{m}_3$	163 949	4608	168 557	173 165
$\boldsymbol{\mu}$, $\boldsymbol{\gamma}$	165 005	4610	169 615	174 225
$\boldsymbol{\mu}$, $\mathbf{m}_4$	155 546	4656	160 202	164 858
$\boldsymbol{\mu}$, $\boldsymbol{\kappa}$	164 717	4610	169 327	173 937
$\boldsymbol{\mu}$, $\boldsymbol{\sigma}_\eta^2$	163 157	4610	167 767	172 377
$\boldsymbol{\mu}$, $\mathbf{K}$	161 244	4612	165 856	170 468
$\boldsymbol{\mu}$, $\boldsymbol{\sigma}^2$, $\mathbf{m}_3$	152 789	4649	**157 438**	**162 087**
$\boldsymbol{\mu}$, $\boldsymbol{\sigma}^2$, $\mathbf{m}_4$	154 361	4658	159 019	163 677
$\boldsymbol{\mu}$, $\boldsymbol{\sigma}^2$, $\boldsymbol{\sigma}_\eta^2$	154 385	4662	159 047	163 709
$\boldsymbol{\mu}$, $\boldsymbol{\sigma}^2$, $\mathbf{K}$	154 318	4656	158 974	163 630
$\boldsymbol{\mu}$, $\boldsymbol{\sigma}^2$, $\mathbf{m}_3$, $\mathbf{m}_4$	152 787	4651	157 438	162 089
$\boldsymbol{\mu}$, $\boldsymbol{\sigma}^2$, $\mathbf{m}_3$, $\boldsymbol{\sigma}_\eta^2$	152 436	4643	157 079	161 722
$\boldsymbol{\mu}$, $\boldsymbol{\sigma}^2$, $\mathbf{m}_3$, $\mathbf{K}$	151 965	4641	***156 606***	***161 247***
$\boldsymbol{\mu}$, $\boldsymbol{\sigma}^2$, $\mathbf{m}_3$, $\mathbf{K}$, $\mathbf{m}_4$	151 583	4644	156 227	160 871
$\boldsymbol{\mu}$, $\boldsymbol{\sigma}^2$, $\mathbf{m}_3$, $\mathbf{K}$, $\boldsymbol{\sigma}_\eta^2$	151 453	4648	**156 101**	**160 749**
$\boldsymbol{\mu}$, $\boldsymbol{\sigma}^2$, $\mathbf{m}_3$, $\mathbf{K}$, $\boldsymbol{\sigma}_\eta^2$, $\mathbf{m}_4$	150 970	4646	**155 616**	**160 262**

accept or reject based on the metropolis rule. Then we Gibbs sample for $\boldsymbol{\beta}_a$ and $\boldsymbol{\beta}_\phi$ and for τ_a and τ_ϕ. After discarding a burn-in period and thinning the remainder, we are left with samples from the joint posterior distribution of the $\boldsymbol{\beta}$s and the τs. The MCMC sampling algorithm implemented in this study is explained in more detail in appendix B and the companion paper OWH; see Coles (2001) and Gelman et al. (2003) for a general discussion on MCMC techniques including the metropolis rule and the Gibbs sampler.

b. Model selection

We have tested different combinations of covariates (i.e., different models) and performed a systematic model selection procedure. The different models are listed in Table 2. The models were compared using the deviance information criteria (DIC; Spiegelhalter et al. 2002), which provides a measure of model fit $\overline{D}$, a measure of model complexity p_D, and the DIC, which is the sum of $\overline{D}$ and p_D. In comparing two models, the one with the lower DIC value is preferred. The model complexity p_D is the effective number of model parameters and provides a penalty for models that may provide a better fit (e.g., a lower $\overline{D}$) but do so without any (or enough) new independent information (e.g., it helps control for model overfitting). However, it should be noted that DIC has a bias toward overfit models (Ando 2007) and so we select our model based on the direct DIC results combined with our background knowledge and expertise in the dynamics of the overall marine climate system.

Model selection was performed using a stepwise regression. We chose the first predictor a priori as the mean SST $\boldsymbol{\mu}$. It is clear from maps of extreme SSTs that the mean SST plays a strong role in determining the pattern of extremes and so we do not feel that this is an improper choice (e.g., cf. Fig. 4, left, and Fig. 2, top left). Each step of the stepwise procedure can be seen as a separate subtable within Table 2, and the DIC score of the best model at each step is shown in bold. We also tested for the power law scaling of certain parameters (e.g., $\boldsymbol{\sigma}^2$ versus $\boldsymbol{\sigma}$, $\mathbf{K}$ versus $\mathbf{K}^{1/2}$, $\boldsymbol{\sigma}_\eta^2$ versus $\boldsymbol{\sigma}_\eta$) but found no significant difference in the DIC scores (not shown).

Note that both skewness $\boldsymbol{\gamma}$ and the third central moment $\mathbf{m}_3$ were considered as possible predictors. Skewness is defined as the third central moment divided by the variance to the power of 3/2 and as such is a unitless quantity (see Table 1). This allows for the relative asymmetry of distributions with different variances to be compared. Here, however, we do not wish to lose information on the magnitude of the distribution asymmetry (in units of $°C^3$), as this will directly impact the magnitude of the extreme values (in units of °C). It can be seen in Table 2 that the model that includes the third central moment is preferable to that which includes the skewness. In fact, the difference in DIC scores is at least as large as the change in DIC between the best models at each step of the stepwise regression. Similar arguments hold for considering both the fourth central moment $\mathbf{m}_4$ and kurtosis $\boldsymbol{\kappa}$ (which is a variance-normalized form of the fourth central moment; see Table 1) and the model comparison similarly shows that the model that includes the fourth central moment is preferable to that which includes the kurtosis (Table 2).

We determined the best model to include $\boldsymbol{\mu}$, $\boldsymbol{\sigma}^2$, $\mathbf{m}_3$, and $\mathbf{K}$ (see DIC score in bolded italics in Table 2). This model was chosen based on the following criteria: (i) the DIC scores have largely converged and the model complexity p_D has reached a minimum at this point in the stepwise regression; (ii) the inclusion of $\mathbf{m}_4$ and $\boldsymbol{\sigma}_\eta^2$ (the next two steps in the stepwise regression) further reduced the DIC scores but we rejected those models based on the fact that they are highly correlated with $\boldsymbol{\sigma}^2$ and $\mathbf{K}$, respectively (correlation coefficients of 0.96 and 0.93 respectively; the correlation coefficients between the remaining covariates range from 0.05 to 0.64); and (iii) we prefer to make a conservative choice based on the fact that DIC scores have a bias toward overfit models (Ando 2007). It is probably best to choose a simpler, if slightly underfit, model than a complex and possibly

overfit model, especially when we apply this model to the A1B experiment (see section 4d). Note that we have also compared the models using the Bayesian predictive information criteria (BPIC; BPIC = $\overline{D} + 2p_D$; Ando 2007), which attempts to compensate for the DIC bias toward overfitting, but it in fact leads to the same conclusions as the DIC (Table 2, last column).

c. Estimates of extreme SSTs for the 1990s

The $\mathbf{z}_{50}$ derived from the CTRL simulation using the BHM (denoted $\mathbf{z}_{50}^{C,H}$) were calculated as the posterior mean of the $\mathbf{z}_{50}$ values sampled using the MCMC technique described above. The $\mathbf{z}_{50}^{C,H}$ exhibit a very similar pattern to $\mathbf{z}_{50}^{\text{obs}}$ (Figs. 4a,b). As above, there is a strong meridional gradient over the entire domain and also a strong zonal gradient between about 25° and 38°S. Also, the spatial pattern of $\mathbf{z}_{50}^{C,H}$ is much smoother than $\mathbf{z}_{50}^{C}$: for example, much of the high wavenumber variability has been removed. We note that this is true even if the climate fields are not smoothed prior to the analysis.

The differences between $\mathbf{z}_{50}^{C,H}$ and $\mathbf{z}_{50}^{\text{obs}}$ are typically less than ±2°C (Fig. 4e). Notably, the model does very well (differences less than ±1°C) over much of the Tasman Sea and the regions adjacent to the Australian land boundary. Differences exceed ±2°C in a small region southeast of Tasmania and in the central eastern portion of the domain that is within the subtropical gyre interior of the southwest Pacific region (see Holbrook and Bindoff 1997). It appears that the BHM may not be capturing the underlying relationship between the central moments and the extremes in these specific regions. However, the BHM does capture this relationship well in much of the Tasman and Coral Seas and near the Australian landmass.

Ideally, before moving on to projecting future extremes in the next section, we would evaluate the model performance against independent data through time (e.g., by splitting the historical record into two or more parts, using bootstrap methods, using hindcast known results, etc.). However, because of the inadequacies of the marine observational record (in record length, data gaps, and spatial and temporal inhomogeneities) and the nature of the analysis of extremes, it is not possible to appropriately split the historical record and evaluate the model in this way, even using a bootstrap-type approach. The historical record comprises 28 yr of data, which translates into annual maxima time series of length 28. We consider this to be a minimum record length against which suitable conclusions can be made about extremal behavior. If we were to split the record into, say, two periods of 14 yr, the periods (i) are unlikely to reflect the overall extremal behavior (because of the short record length) and (ii) are highly likely to have significantly different extremal statistics (because of their small sample sizes) despite nearly identical background climates. Alternatively, bootstrapping is inappropriate as the fitting and validation datasets should contain the same number of data points in order to be able to compare the statistics of their extremes. Therefore, in the absence of a longer observational record, we are unfortunately unable to perform an appropriate or robust evaluation of the model results through time.

Instead, we have applied a relatively simple spatial cross-validation approach to evaluate the model performance against independent data. We have split the spatial domain into two regions: a training region and a validation region. The definition of the training and validation regions was free and we chose a structured twofold cross-validation procedure. A checkerboard pattern, with squares of side length $L = 15°$ latitude and longitude (see appendix C for details on the choice of this length scale), was defined over the entire domain. For the first validation test, the training region consists of the black squares and the validation region consists of the white squares (Fig. 5b); for the second test, the training and validation regions are switched (Fig. 5c). A checkerboard pattern, as opposed to simply dividing the domain into two along a central east–west or north–south line, was chosen so that all physical regions (tropics, Southern Ocean, western boundary current, subtropical gyre, etc.) are included in the model. By comparing the 50-yr return levels over the validation regions of Figs. 5b and 5c (the nonstippled regions) against the same region in the observations (Fig. 5a), we can see that the BHM performs well at capturing the spatial pattern of the extreme SSTs. We have confirmed that the BHM has successfully used the extremes–covariate relationship to realistically estimate extreme SSTs outside the training region.

d. Estimating extreme SSTs for the 2060s

We have demonstrated that the BHM approach has provided improved estimates of SST extremes over those estimates obtained by directly fitting the Gumbel distribution to the CTRL simulation annual maxima. We now take the fitted model from section 4b and use it to estimate extreme SSTs for the 2060s based on the A1B emissions scenario simulation. We do so by using the same regression coefficients and error variances (the $\boldsymbol{\beta}$s and τs) and swapping the CTRL simulation covariates $\boldsymbol{X}$ for those derived from the A1B simulation. In this way, we can generate samples from the posterior distributions of $\mathbf{a}$, $\mathbf{b}$, and $\mathbf{z}_{50}$ that are representative of the A1B scenario marine climate.

The $\mathbf{z}_{50}$ posterior mean from the A1B simulation using the BHM (denoted as $\mathbf{z}_{50}^{A,H}$) is shown in Fig. 6b along

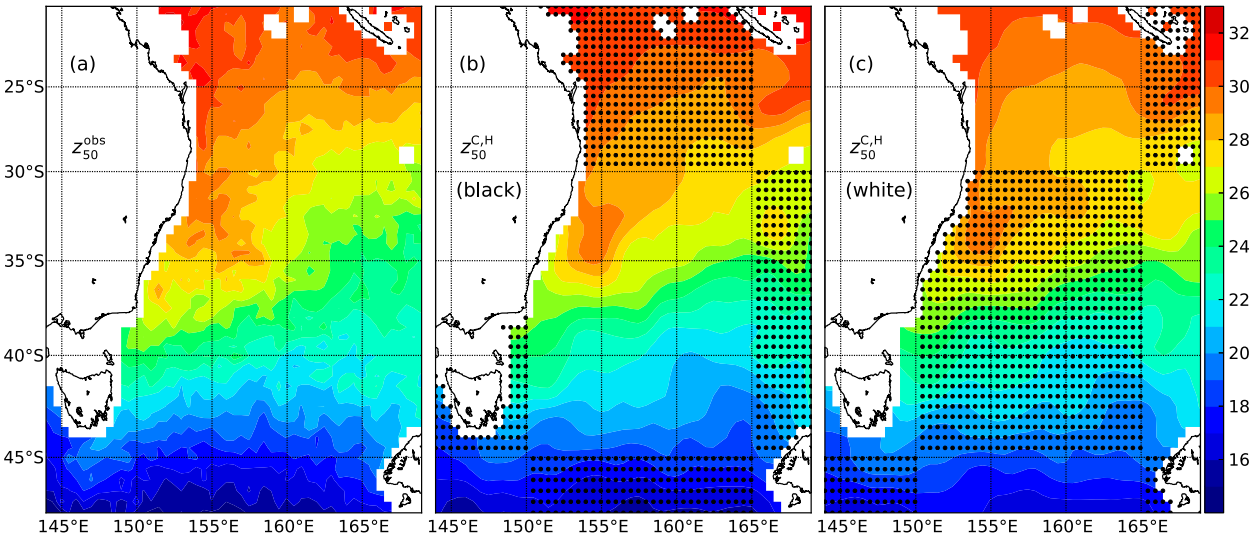

FIG. 5. Cross validation of BHM extremes model. (a) The 50-yr return level extreme SSTs from observations ($\mathbf{z}_{50}^{obs}$). (b),(c) The 50-yr return levels from the cross validation of the BHM extremes model for the 1990s ($\mathbf{z}_{50}^{C,H}$). In (b), the model has been trained over the black checkerboard squares, indicated by stippling, and then used to predict over the white checkerboard squares. In (c), the model has been trained on the white checkerboard squares, again indicated by the stippling, and used to predict over the black checkerboard squares.

with $\mathbf{z}_{50}^{C,H}$ in Fig. 6a. The pattern of extreme SSTs is similar: a strong meridional gradient over the whole domain and a strong zonal gradient between about 25° and 38°S. However, the absolute values of $\mathbf{z}_{50}^{A,H}$ are larger than $\mathbf{z}_{50}^{C,H}$. The difference (Fig. 6c) shows that the $\mathbf{z}_{50}$ values are at least 1°C greater over almost the entire domain. In addition, there is a ''hotspot'' in the central and western Tasman Sea where the $\mathbf{z}_{50}$ values are 2°–4°C greater in $\mathbf{z}_{50}^{A,H}$ than in $\mathbf{z}_{50}^{C,H}$.

The Bayesian approach underlying the BHM provides information about the entire posterior distribution and not only the posterior mean. This information can be used to provide probabilistic information about the change in SST extremes between the 1990s and 2060s. From the posterior samples of **a** and **b**, we can sample from the posterior distribution of the annual maxima **Y**: essentially simulations of extreme SSTs. This is undertaken for both the CTRL and A1B simulations. Therefore, at

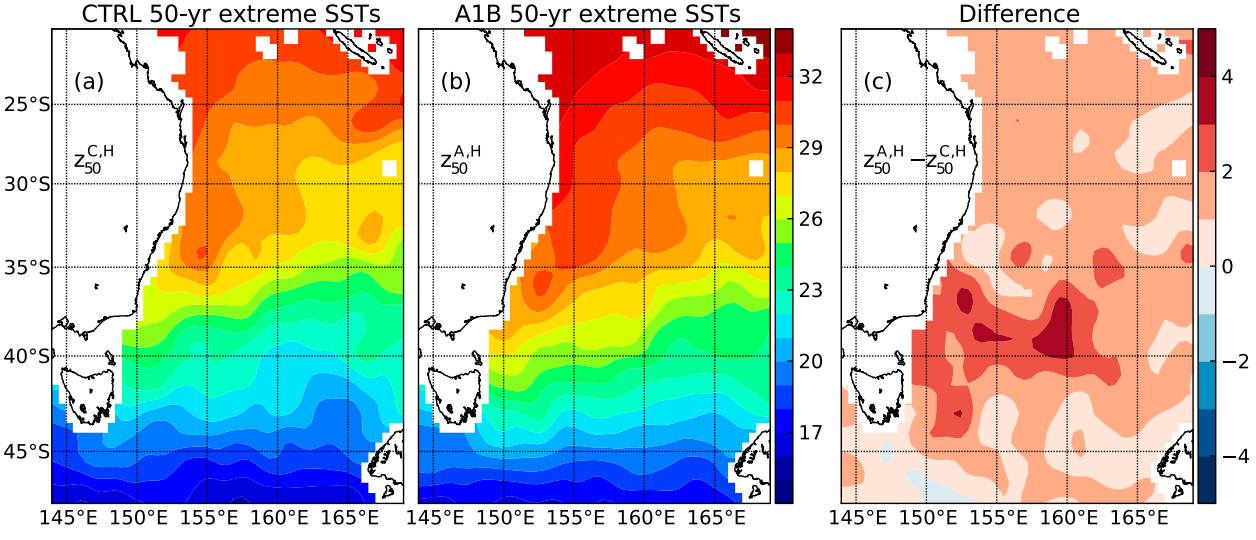

FIG. 6. The 50-yr return levels for the (left) CTRL ($\mathbf{z}_{50}^{C,H}$) and (middle) A1B ($\mathbf{z}_{50}^{A,H}$) simulation sea surface temperatures using the Bayesian hierarchical model. The return levels are calculated from the mean of the posterior distributions for the 50-yr return levels. (right) The difference between the 50-yr return levels of the two simulations is shown.

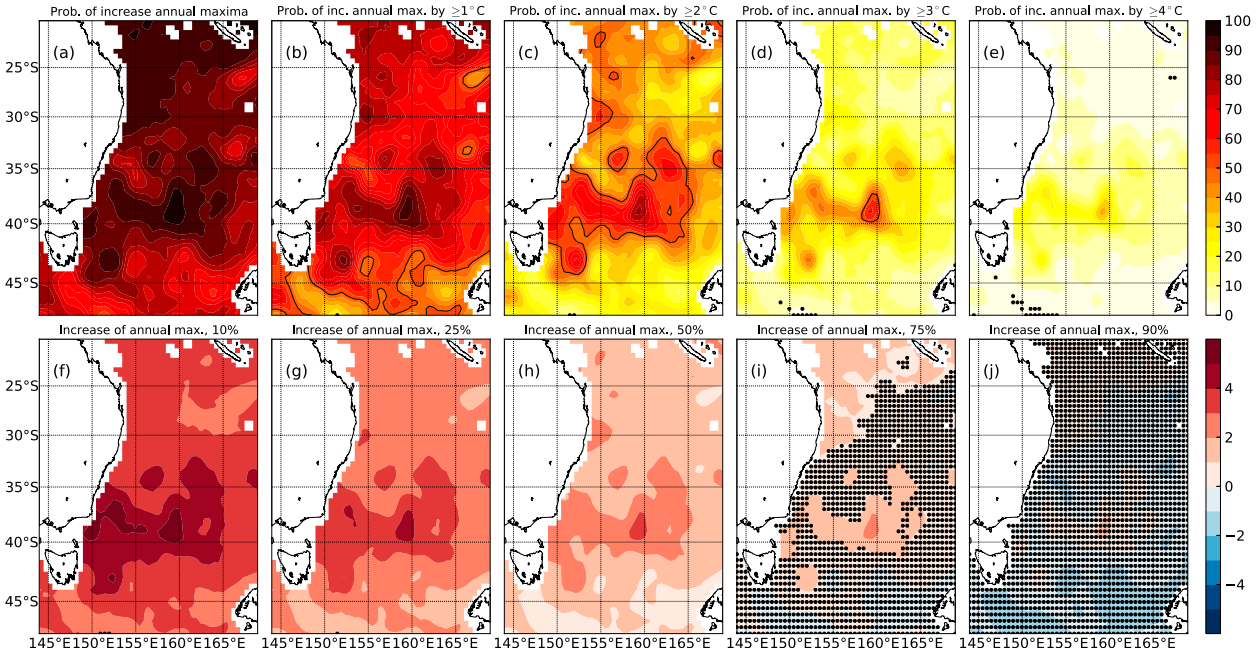

FIG. 7. Probabilities of change in annual maxima. (top) Contours indicate (a) the probabilities that the maximum annual SSTs will increase by any amount between the 1990s and 2060s and the probabilities that they will increase by at least (b)–(e) 1°, 2°, 3°, and 4°C. Black dots indicate where these probabilities do not exceed those due to randomness in an unchanged climate. (bottom) Contours indicate the minimum changes in annual maxima estimated with probabilities of (f)–(j) 10%, 25%, 50%, 75%, and 90%. The black dots indicate that the minimum changes do not exceed those due to randomness in an unchanged climate.

each location in space we have a sample of 6000 (see appendix B) annual maxima under the CTRL and the A1B climates, and from these we can calculate probabilities of changes in annual maxima.

Spatial maps of the probability distributions are provided in Fig. 7. These are probabilities that SST annual maxima will increase by a specified amount, based on the posterior samples, between the 1990s and the 2060s. The probabilities that annual maxima will increase by any amount between the 1990s and the 2060s is at least 50% over almost the entire domain (Fig. 7a). The probabilities that annual maxima will increase by at least 1°, 2°, 3°, or 4°C (Figs. 7b–e) highlights the Tasman Sea hotspot noted above. For example, the probability that extremes will increase across this southwest Pacific domain is close to 100% everywhere across both the central Tasman Sea and the Coral Sea (Fig. 7a). However, as we increase the threshold from at least 1°C to at least 3°C (Fig. 7d), the probabilities in the Coral Sea have dropped to less than 20%, while in the central Tasman Sea they remain as high as 40%–60%.

The same information can be inverted to provide a different perspective, as shown in Figs. 7f–j. Here, each panel maps the minimum change in annual maxima, between the 1990s and the 2060s, at the indicated threshold probability. With a 10% probability (i.e., very unlikely), we see minimum changes in annual maxima of over 3°C over much of the domain and exceeding 4°–5°C in some regions (Fig. 7f). As we increase the probabilities to 25%, 50%, 75%, and 90% (i.e., go from less to more likely; Figs. 7g–j), the estimates become increasingly more conservative and the change in annual maxima progressively decreases as expected.

We can compare these estimates against what can be expected randomly given an unchanged climate (i.e., the 1990s climate from the CTRL simulation). The black dots in the top panels of Fig. 7 indicate where the probabilities are no greater than the probabilities of the same increase in annual maxima from two samples drawn from the posterior distribution given the 1990s climate: that is, a null hypothesis of no climate change. The vast majority of locations (with the exception of a few in the extreme south and northeast of the domain in Figs. 7d,e) have probabilities exceeding those expected randomly in an unchanged climate for a ≥4°C increase in annual maxima (Fig. 7e).

In the bottom panels of Fig. 7, the black dots indicate where the minimum changes in annual maxima are no greater than those expected randomly from the CTRL climate. Therefore, with 90% probability we can say very little about our estimated changes relative to what can be expected by random chance in an unchanged climate

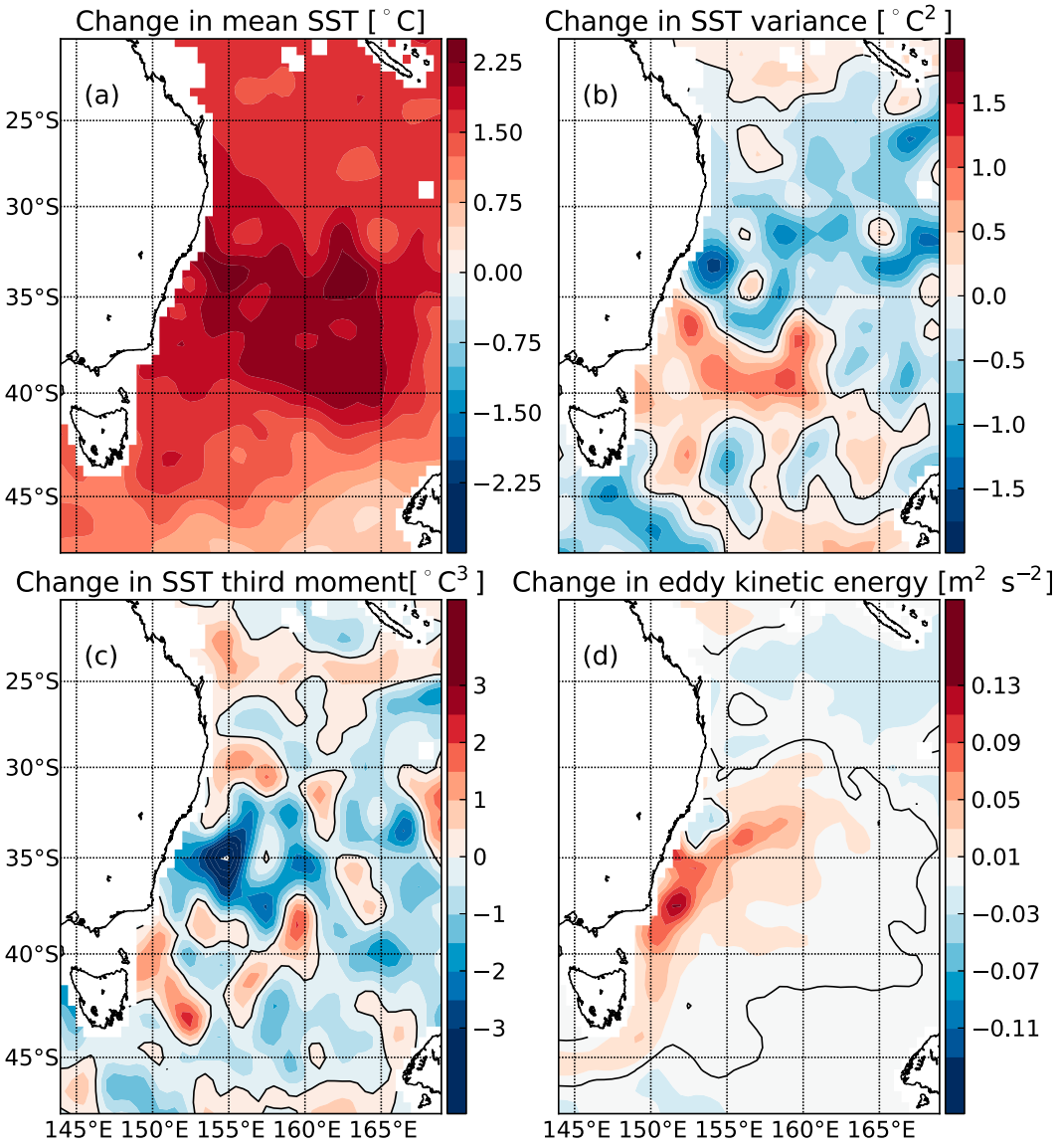

FIG. 8. Changes in various marine climate statistics. Shown are the differences between A1B and CTRL simulation (a) mean SST, (b) SST variance, (c) SST third central moment, and (d) eddy kinetic energy.

(Fig. 7j). However, we can claim that our model estimates a 75% probability of minimum changes in annual maxima in the Tasman Sea hotspot of ≥2°C (Fig. 7i) and a 50% probability of minimum changes in annual maxima over most of 1°–2°C over most of the domain and 2°–4°C in the Tasman Sea hotspot.

e. *Relating the change in extremes to marine climate change*

The presence of this hotspot of change in extreme SSTs indicates that the extremes are not changing uniformly in space. We have examined this by mapping the change in individual marine climate statistics between the A1B and CTRL simulations. The mean SST is projected to increase over the entire domain, with a hotspot in the upper central Tasman Sea (Fig. 8a). The overall positive change in mean SST clearly contributes to the fact that the change in $\mathbf{z}_{50}$ is positive over nearly the entire domain. However, the hotspot of mean SST change (upper central Tasman Sea) is not collocated with the hotspot of change in extremes (central and western Tasman Sea; cf. Figs. 6c, 8a). Further, the SST variance is projected to increase over a region of similar extent to the extremes hotspot and decrease farther north (Fig. 8b). The SST third central moment is projected to increase east of Tasmania and largely decrease farther north (Fig. 8c). A comparison of these last two patterns with the pattern of change in $\mathbf{z}_{50}$ shows much in common. Therefore, it appears that the

change in extreme SSTs in a changing climate is due largely to a combination of changes to the mean SST, SST variance, and the SST third central moment.

The change in eddy kinetic energy shows a broad region of positive change in the Tasman Sea, which is intensified near the Australian coast and south of the EAC separation zone (Fig. 8d). This pattern does not match the pattern of change in $\mathbf{z}_{50}$ but may be indicative of an underlying mechanism: that is, an increased level of eddy activity in the Tasman Sea leading to an increased variability of SST (more eddies moving in space and time) and an increased SST skewness (more warm-core eddies).

5. Summary and discussion

The aim of this study was to estimate extreme sea surface temperature (SST) events off southeastern Australia for the decades of the 1990s and 2060s, under a climate change emissions scenario. Such estimations were felt to be important for two main reasons. First, existing atmosphere and ocean general circulation models—and global climate models especially—tend to have a poor representation of extremes and thus an improvement upon this would be a valuable and useful contribution. Second, extreme events in the marine environment have not been studied extensively and are particularly important for ecology. Extreme marine conditions can have harmful or even devastating effects on habitat distribution. We feel that this study begins to fill in the present need for more accurate estimates of extremes in the marine environment in a changing global climate.

We estimated extreme SSTs from observations and from the dynamically downscaled OFAM CTRL simulation, representing the 1990s, by fitting an extreme value distribution (the Gumbel distribution) to observed and simulated SST annual maxima. While the CTRL simulation provided reasonable estimates of extreme SSTs (differences between observed and simulated 50-yr return levels were typically less than ±3°–4°C), we felt that this result could be improved upon. Therefore, we developed a Bayesian hierarchical model (BHM), informed by the CTRL simulation marine climate, to improve the estimation of observed extreme SSTs. This model provided improved estimates of SSTs for the 1990s (differences between observed and simulated 50-yr return levels were typically less than ±2°C).

This fitted model was then applied to output from a corresponding dynamically downscaled simulation of an A1B climate, representing the 2060s under a climate change scenario, to provide estimates of future extreme SSTs. The estimated change in extreme SSTs between the 1990s and the 2060s from the BHM extreme value model highlights the presence of a projected hotspot in the southwestern Tasman Sea, where the change in extreme SSTs is greater than in the surrounding region.

We have shown that the pattern of SST extremes can be reasonably well represented using only the key central statistics, or the marine climate. The basic pattern of SST extremes is dominated by the mean SST; the SST variance also plays a strong role especially near the EAC separation zone. The climate variables have different patterns of change between the 1990s and the 2060s, e.g., the mean SST increases everywhere with a hotspot in the central Tasman Sea while the variance increases in the southwestern Tasman Sea and decreases immediately to the north. Therefore, changes in the extremes are a result of a combination of changes in the marine climate statistics.

We estimate the extreme SSTs off southeastern Australia to change significantly between the 1990s and the 2060s. The 50-yr return period extremes are projected to increase by up to 2°C over almost the entire domain, excluding the extreme south. In addition, 50-yr return levels in a hotspot region identified in the central and western Tasman Sea are projected to increase by 2°–4°C because of changes in the SST variability in that region. The Bayesian approach has given us probabilistic information about the changes as well. The probability that annual maxima in the 2060s will be warmer than in the 1990s is >50% across the entire domain; the probability that the hotspot will be >2°C is over 50%. These results exceed random effects in an unchanged climate and therefore there is some evidence that anthropogenic climate change is significantly influencing the projected SSTs.

Possible mechanisms for the observed changes in extremes are twofold. First, the mean SST is increasing nearly everywhere because of an overall warming climate. There is also a hotspot of increasing mean SST (Holbrook and Bindoff 1997; Ridgway 2007) and it has been suggested that its presence is related to a stronger EAC transporting more warm water into the Tasman Sea (Ridgway 2007). Second, the changes in the variance (and possibly the third central moment as well) are most likely due to changes in eddy activity. The eddy kinetic energy, especially near the coast of southeastern Australia, is simulated to increase dramatically between the 1990s and 2060s (by up to 100% or more in some regions). Matear et al. (2013) have noted a projected increase of eddy activity in the Tasman Sea in these dynamically downscaled simulations and linked it to increased nutrient levels because of enhanced vertical mixing. This may be due to increased numbers of eddies and/or more stable (long lived) eddies due to a more stable stratification in a warmer climate.

In this study, we have examined extremes using marine climate projections from a single model configuration. We recognize that there would be utility in examining results and BHM behavior across several model configurations. However, there are larger philosophical and practical questions around doing this in our opinion, which places it beyond the scope of the present study. Consider the BHM applied to output from a suite of climate models. If the bias correction from our extremes model worked perfectly, then the results for the historical period from all models would be the same and equal to the observed extremes. In reality, however, the bias correction will not work perfectly (as is in fact the case for the model considered in the present study; see Fig. 4e) and results will differ between models and observations, as well as across models. These differences could be interpreted, correctly, in two ways: (i) as failings in the BHM extremes model or (ii) as failings in the climate models themselves (or both). Differences may arise because of significant failings in the climate models because of their inability to capture a particular aspect of the marine climate (e.g., the distribution of SST variance could be completely wrong). While bias correcting should improve any model, it cannot work miracles if marine climate estimates are too far different from observations. Differences may also arise because of failings of the BHM extremes model itself: that is, an inability to effectively perform the bias correction. A comprehensive analysis of differences across bias-corrected model results is a considerable undertaking and requires a separate study.

The Bayesian hierarchical extreme value technique used in this study provides a framework for estimating realistic and robust extremes from climate or ocean model outputs that do not adequately reproduce the extremes. Essentially, the model is a form of bias correction. The observed extremes are used to calibrate the model of extremes from marine climate simulations over the same period and this bias correction is then applied to the simulation of future climate. This approach is general and can be applied to other marine (e.g., salinity, chlorophyll) or atmospheric (e.g., air temperature, precipitation) variables. To use this technique for a chosen marine or atmospheric variable, the following two conditions must be satisfied: First, observations of extreme values and model simulations of climate statistics must be available over the same time period (typically the present but possibly a historical time period). Second, model simulations of climate statistics must be available for another time period for which projections of extremes are desired (typically a future projection). The technical details of this approach are described in more detail by OWH.

Acknowledgments. The authors would like to acknowledge funding from the Australian Research Council Super Science Fellowship (Grant FS110200029). The authors acknowledge Richard Matear of CSIRO Marine and Atmospheric Research (Hobart, Australia) for helpful discussions and for providing the OFAM model output. The sea surface temperature observations were provided by GHRSST and the U.S. National Oceanographic Data Center, and that project was supported in part by a grant from the NOAA Climate Data Record (CDR) Program for satellites. The altimeter products were produced by Ssalto/Duacs and distributed by AVISO with support from CNES. This manuscript makes a contribution to objectives of the ARC Centre of Excellence for Climate System Science (ARC CoE CCS) and the CLIVAR-endorsed Southwest Pacific Ocean Circulation and Climate Experiment (SPICE).

APPENDIX A

The Bayesian Hierarchical Model

We model the extreme SSTs using a Bayesian hierarchical model (BHM). The BHM is described in detail in OWH, and here we present an overview sufficient for the present study. Any reader wishing to develop a similar model or gain further insight into the technique should consult OWH.

There are three layers in our BHM. The data layer models the observed annual maxima $\mathbf{Y}$ using the Gumbel distribution. The climate process layer models the parameters of the Gumbel distribution $\boldsymbol{\theta}_2$ as functions of a latent spatial process described in terms of marine climate variables. The final layer consists of the prior distributions for the parameters of the climate process layer $\boldsymbol{\theta}_1$. In this way, the inference for the parameters of the climate process model is given by Bayes rule,

$$p(\boldsymbol{\theta} \mid \mathbf{Y}) \propto p(\mathbf{Y} \mid \boldsymbol{\theta}_2) p(\boldsymbol{\theta}_2 \mid \boldsymbol{\theta}_1) p(\boldsymbol{\theta}_1), \tag{A1}$$

where $p(\boldsymbol{\theta} \mid \mathbf{Y})$ is the posterior distribution of $\boldsymbol{\theta} = (\boldsymbol{\theta}_1, \boldsymbol{\theta}_2)$ given the data $\mathbf{Y}$, $p(\mathbf{Y} \mid \boldsymbol{\theta}_2)$ is the likelihood function (i.e., the Gumbel distribution extreme value model), $p(\boldsymbol{\theta}_2 \mid \boldsymbol{\theta}_1)$ is the climate process model, and $p(\boldsymbol{\theta}_1)$ are the priors. Samples from the posterior distribution of $\boldsymbol{\theta}$ are estimated using a Markov chain Monte Carlo algorithm described in appendix B.

a. Data layer

We assume that, at each location j, the annual maxima $\mathbf{y}_j$ are distributed according to the Gumbel distribution [see Eq. (3)],

$$p(\mathbf{y}_j \mid a_j, \phi_j) = \prod_{i=1}^{n} f_{\mathrm{I}}(y_{ji} \mid a_j, \phi_j), \tag{A2}$$

where n is the number of annual maxima (i.e., $\mathbf{y}_j$ is a vector of length n); f_{I} is the Gumbel density function; and the scale parameter b_j has been scaled logarithmically, $\phi_j = \log(b_j)$, to allow for both positive and negative values in the model. When considering annual maxima at all locations $\mathbf{Y} = \{\mathbf{y}_j \mid j = 1, 2, \ldots, J\}$, the probability becomes

$$p(\mathbf{Y} \mid \boldsymbol{\theta}_2) = \prod_{j=1}^{J} p(\mathbf{y}_j \mid a_j, \phi_j) = \prod_{j=1}^{J} \prod_{i=1}^{n} f_{\mathrm{I}}(y_{ji} \mid a_j, \phi_j), \tag{A3}$$

where $\boldsymbol{\theta}_2 = (\mathbf{a}, \phi)$; $\mathbf{a} = \{a_j \mid j = 1, 2, \ldots, J\}$; and $\phi = \{\phi_j \mid j = 1, 2, \ldots, J\}$.

b. Climate process layer

We assume the model for the Gumbel parameters $\boldsymbol{\theta}_2$ can be factored into independent models for $\mathbf{a}$ and ϕ: that is,

$$p(\boldsymbol{\theta}_2 \mid \boldsymbol{\theta}_1) = p(\mathbf{a} \mid \boldsymbol{\theta}_{1,a}) p(\phi \mid \boldsymbol{\theta}_{1,\phi}), \tag{A4}$$

where $\boldsymbol{\theta}_1 = (\boldsymbol{\theta}_{1,a}, \boldsymbol{\theta}_{1,\phi})$.

We model the parameters $\mathbf{a}$ and ϕ as multivariate normal distributions with means that are linear combinations of some covariates [see Eqs. (6) and (7)],

$$p(\mathbf{a} \mid \boldsymbol{\theta}_{1,a}) = \mathcal{N}_J(\mathbf{X}\boldsymbol{\beta}_a, \tau_a^{-1}\mathbf{I}) \quad \text{and} \tag{A5}$$

$$p(\phi \mid \boldsymbol{\theta}_{1,\phi}) = \mathcal{N}_J(\mathbf{X}\boldsymbol{\beta}_\phi, \tau_\phi^{-1}\mathbf{I}). \tag{A6}$$

Here, $\mathbf{X}$ is a $J \times M$ design matrix of covariates (X_{jm} is the value of the mth covariate at location j), $\boldsymbol{\beta}_a$ and $\boldsymbol{\beta}_\phi$ are $M \times 1$ vectors of regression coefficients, and τ_a and τ_ϕ are error precisions. Here, M is the number of covariate variables plus one: each variable corresponds to a column of $\mathbf{X}$ and is defined at all locations j and the plus one indicates the required column of ones in $\mathbf{X}$ [see Eq. (8)]. The parameters of the climate process layer are $\boldsymbol{\theta}_1 = (\boldsymbol{\beta}_a, \boldsymbol{\beta}_\phi, \tau_a, \tau_\phi)$.

c. Priors

We assume that each parameter in the climate process layer is distributed independently: that is,

$$p(\boldsymbol{\theta}_1) = p(\boldsymbol{\beta}_a) p(\boldsymbol{\beta}_\phi) p(\tau_a) p(\tau_\phi). \tag{A7}$$

The following forms have been assumed for the priors of each of these parameters:

$$p(\boldsymbol{\beta}_a) = \mathcal{N}_M(\boldsymbol{\mu}_a, \tau_{a,0}\mathbf{I}), \tag{A8}$$

$$p(\boldsymbol{\beta}_\phi) = \mathcal{N}_M(\boldsymbol{\mu}_\phi, \tau_{\phi,0}\mathbf{I}), \tag{A9}$$

$$p(\tau_a) = \mathrm{Gamma}(\alpha_a, \theta_a), \quad \text{and} \tag{A10}$$

$$p(\tau_\phi) = \mathrm{Gamma}(\alpha_\phi, \theta_\phi), \tag{A11}$$

where $\boldsymbol{\mu}_a = \boldsymbol{\mu}_\phi = 0$, $\tau_{a,0} = \tau_{\phi,0} = 10^{-2}$, $\alpha_a = \alpha_\phi = 10$, and $\theta_a = \theta_\phi = 1$ are chosen to provide suitably broad (diffuse) priors.

APPENDIX B

Markov Chain Monte Carlo Sampling

Samples from the posterior distribution $p(\boldsymbol{\theta} \mid \mathbf{Y})$ are generated using a Markov chain Monte Carlo (MCMC) algorithm. Initially, the parameter values are set to $\boldsymbol{\theta}_1 = (\boldsymbol{\beta}_a, \boldsymbol{\beta}_\phi, \tau_a, \tau_\phi) = (\mathbf{0}, \mathbf{0}, 1, 1)$ and $\boldsymbol{\theta}_2 = (\mathbf{a}, \phi) = (\mathbf{0}, \mathbf{0})$. Then, at each step of the MCMC loop:

1) Loop over all locations $j = 1, 2, \ldots J$ and for each j:
   (i) Draw candidate samples of a_j and ϕ_j using Eqs. (A5) and (A6).
   (ii) Accept or reject candidates based on the Metropolis rule (e.g., Gelman et al. 2003).
2) Given $\mathbf{a}$ and $\boldsymbol{\phi}$ (at all locations), Gibbs sample for the $\boldsymbol{\beta}$s and τs. This step requires that expressions for the conditional distributions for the $\boldsymbol{\beta}$s and τs be known explicitly. These are supplied by OWH.

The MCMC loop is performed for 100 000 iterations. We thin the chain, retaining every 10th sample, and discard a burn-in period of 4000 samples to yield $N = 6000$ samples from the posterior.

We can use samples of $\boldsymbol{\theta}_1$ to generate samples from the posterior predictive distributions of $\mathbf{a}$ and ϕ [see Eqs. (A5) and (A6)] and, given a return period L, the return levels $\boldsymbol{z}_L$ [see Eqs. (4) and (5)]. Then, given samples of $\mathbf{a}$ and ϕ (and $\mathbf{b} = \exp\phi$), we can generate samples from the posterior distribution of the annual maxima $\mathbf{Y}$ [see Eqs. (3) and (A3)]. Given samples from such distributions, it is straightforward to calculate posterior means, variances, and other statistical measures.

APPENDIX C

Correlation Length Scale of SST Extremes

In this appendix, we describe the method used to determine the checkerboard side length L used in the spatial cross-validation procedure in section 4c. Since there

is serial correlation (spatially) of the SST annual maxima time series, the choice of L is important: L must be larger than the spatial correlation length scale to ensure that the data in the training and validation regions are independent.

We determine the correlation length scale as follows: The elements of the cross-correlation matrix $\mathbf{R}$ for the SST annual maxima $\mathbf{Y}$ are given by $R_{ij} = \rho(\mathbf{y}_i, \mathbf{y}_j)$, where $\rho(\mathbf{x}, \mathbf{y})$ represents the zero-lag correlation between time series $\mathbf{x}$ and $\mathbf{y}$. We modeled the spatial structure of the cross correlation as a two-dimensional Gaussian $\mathbf{G}$ [following Meyers et al. (1991) and Holbrook and Bindoff (2000)],

$$G_{ij} = \exp\left[-\frac{(x_{1i} - x_{1j})^2}{L_1^2} - \frac{(x_{2i} - x_{2j})^2}{L_2^2}\right], \quad \text{(C1)}$$

where L_1 and L_2 are the zonal and meridional correlation length scales, respectively. If we take the logarithm of G_{ij}, we have

$$\log G_{ij} = -\frac{(x_{1i} - x_{1j})^2}{L_1^2} - \frac{(x_{2i} - x_{2j})^2}{L_2^2} = K_1 X_{1ij} + K_2 X_{2ij}, \quad \text{(C2)}$$

where $K_1 = -L_1^2, K_2 = -L_2^2, X_{1ij} = (x_{1i} - x_{1j})^2$, and $X_{2ij} = (x_{2i} - x_{2j})^2$, which is linear in $\mathbf{X}_1$ and $\mathbf{X}_2$. We fit this Gaussian to $\mathbf{R}$ by linear regression,

$$\text{vec}(\log\mathbf{R}) = K_1 \text{vec}(\mathbf{X}_1) + K_2 \text{vec}(\mathbf{X}_2) + \boldsymbol{\epsilon}, \quad \text{(C3)}$$

where vec denotes the vectorization of a matrix by sequentially stacking the columns on one another (e.g., Harvey 1990) and ϵ is an error term. Least squares estimates of K_1 and K_2 lead to correlation length scale estimates of $L_1 = 13.2°$ and $L_2 = 14.8°$. Therefore, we took $L = 15° > L_2 > L_1$ as our estimate of the checkerboard side length.

REFERENCES

Alexander, L. V., and Coauthors, 2006: Global observed changes in daily climate extremes of temperature and precipitation. *J. Geophys. Res.,* **111,** D05109, doi:10.1029/2005JD006290.

Andersen, O. B., and P. Knudsen, 2009: DNSC08 mean sea surface and mean dynamic topography models. *J. Geophys. Res.,* **114,** C11001, doi:10.1029/2008JC005179.

Ando, T., 2007: Bayesian predictive information criterion for the evaluation of hierarchical Bayesian and empirical Bayes models. *Biometrika,* **94,** 443–458.

Ballester, J., F. Giorgi, and X. Rodó, 2010: Changes in European temperature extremes can be predicted from changes in PDF central statistics. *Climatic Change,* **98,** 277–284.

Berman, S. M., 1964: Limit theorems for the maximum term in stationary sequences. *Ann. Math. Stat.,* **35,** 502–516.

Bernier, N. B., and K. R. Thompson, 2006: Predicting the frequency of storm surges and extreme sea levels in the northwest Atlantic. *J. Geophys. Res.,* **111,** C10009, doi:10.1029/2005JC003168.

Brassington, G. B., N. Summons, and R. Lumpkin, 2011: Observed and simulated Lagrangian and eddy characteristics of the East Australian Current and the Tasman Sea. *Deep-Sea Res. II,* **58,** 559–573.

Caires, S., and A. Sterl, 2005: 100-year return value estimates for ocean wind speed and significant wave height from the ERA-40 data. *J. Climate,* **18,** 1032–1048.

Carter, D., J. Loyens, and P. Challenor, 1987: Estimates of extreme current speeds over the continental slope off Scotland. Institute of Oceanographic Sciences Rep. 239, 290 pp.

Chamberlain, M. A., C. Sun, R. J. Matear, M. Feng, and S. J. Phipps, 2012: Downscaling the climate change for oceans around Australia. *Geosci. Model Dev. Discuss.,* **5,** 425–458.

Church, J. A., J. R. Hunter, K. L. McInnes, and N. J. White, 2006: Sea-level rise around the Australian coastline and the changing frequency of extreme sea-level events. *Aust. Meteor. Mag.,* **55,** 253–260.

Coles, S., 2001: *An Introduction to Statistical Modeling of Extreme Values.* Springer, 208 pp.

——, and D. Walshaw, 1994: Directional modelling of extreme wind speeds. *Appl. Stat.,* **43,** 139–157.

——, and J. A. Tawn, 1996: A Bayesian analysis of extreme rainfall data. *Appl. Stat.,* **45,** 463–478.

Cook, N., 1985: *The Designer's Guide to Wind Loading of Building Structures. Part 1: Background Damage Survey, Wind Data and Structural Classification.* Building Research Establishment, Garston, and Butterworths, 383 pp.

Cooley, D., D. Nychka, and P. Naveau, 2007: Bayesian spatial modeling of extreme precipitation return levels. *J. Amer. Stat. Assoc.,* **102,** 824–840.

Cressie, N., and C. K. Wikle, 2011: *Statistics for Spatio-Temporal Data.* Wiley, 588 pp.

Dawson, T., 2000: Maximum wave crests in heavy seas. *J. Offshore Mech. Arctic Eng.,* **122,** 222–224.

de Vries, H., R. J. Haarsma, and W. Hazeleger, 2012: Western European cold spells in current and future climate. *Geophys. Res. Lett.,* **39,** L04706, doi:10.1029/2011GL050665.

Dixon, M., J. Tawn, and J. Vassie, 1998: Spatial modelling of extreme sea-levels. *Environmetrics,* **9,** 283–301.

Gelman, A., J. B. Carlin, H. S. Stern, and D. B. Rubin, 2003: *Bayesian Data Analysis.* 2nd ed. CRC Press, 696 pp.

Godfrey, J. S., G. R. Cresswell, T. J. Godling, A. F. Pearce, and R. Boyd, 1980: The separation of the East Australian Current. *J. Phys. Oceanogr.,* **10,** 430–440.

Griffiths, C. R., 1996: Extreme residual current speeds upon the UK continental shelf. Health and Safety Executive Offshore Tech. Rep. OTH94/437, 53 pp.

Griffiths, G. M., and Coauthors, 2005: Change in mean temperature as a predictor of extreme temperature change in the Asia–Pacific region. *Int. J. Climatol.,* **25,** 1301–1330.

Gumbel, E., 1941: The return period of flood flows. *Ann. Math. Stat.,* **12,** 163–190.

——, 1958: *Statistics of Extremes.* Columbia University Press, 375 pp.

Harvey, A., 1990: Forecasting, Structural Time Series Models and the Kalman Filter. Cambridge University Press, 554 pp.

Hennessey, J., 1977: Some aspects of wind power statistics. *J. Appl. Meteor.,* **16,** 119–128.

Holbrook, N. J., and N. L. Bindoff, 1997: Interannual and decadal temperature variability in the southwest Pacific Ocean between 1955 and 1988. *J. Climate,* **10,** 1035–1049.

——, and ——, 2000: A statistically efficient mapping technique for four-dimensional ocean temperature data. *J. Atmos. Oceanic Technol.,* **17,** 831–846.

Hunter, J., 2010: Estimating sea-level extremes under conditions of uncertain sea-level rise. *Climatic Change,* **99,** 331–350.

Kharin, V., F. Zwiers, X. Zhang, and G. Hegerl, 2007: Changes in temperature and precipitation extremes in the IPCC ensemble of global coupled model simulations. *J. Climate,* **20,** 1419–1444.

Matear, R. J., M. A. Chamberlain, C. Sun, and M. Feng, 2013: Climate change projection of the Tasman Sea from an eddy-resolving ocean model. *J. Geophys. Res.,* **118,** 2961–2976.

McGuffie, K., A. Henderson-Sellers, N. Holbrook, Z. Kothavala, O. Balachova, and J. Hoekstra, 1999: Assessing simulations of daily temperature and precipitation variability with global climate models for present and enhanced greenhouse climates. *Int. J. Climatol.,* **19,** 1–26.

Mearns, L. O., R. W. Katz, and S. H. Schneider, 1984: Extreme high-temperature events: Changes in their probabilities with changes in mean temperature. *J. Climate Appl. Meteor.,* **23,** 1601–1613.

Meyers, G., H. Phillips, N. Smith, and J. Sprintall, 1991: Space and time scales for optimal interpolation of temperature—Tropical Pacific Ocean. *Prog. Oceanogr.,* **28** (3), 189–218.

Muir, L. R., and A. El-Shaarawi, 1986: On the calculation of extreme wave heights: A review. *Ocean Eng.,* **13,** 93–118.

Oke, P. R., G. B. Brassington, D. A. Griffin, and A. Schiller, 2008: The Bluelink ocean data assimilation system (BODAS). *Ocean Modell.,* **21** (1–2), 46–70.

Oliver, E. C. J., and N. J. Holbrook, 2014: A statistical method for improving continental shelf and near-shore marine climate predictions. *J. Atmos. Oceanic Technol.,* **31,** 216–232.

——, J. Sheng, K. R. Thompson, and J. R. U. Blanco, 2012: Extreme surface and near-bottom currents in the northwest Atlantic. *Nat. Hazards,* **64,** 1425–1446.

——, S. J. Wotherspoon, and N. J. Holbrook, 2014: Estimating extremes from global ocean and climate models: A Bayesian hierarchical model approach. *Prog. Oceanogr.,* doi:10.1016/j.pocean.2013.12.004, in press.

Pearce, A., and M. Feng, 2012: The rise and fall of the ''marine heat wave'' off Western Australia during the summer of 2010/11. *J. Mar. Syst.,* **111–112,** 139–156.

Perkins, S. E., A. J. Pitman, N. J. Holbrook, and J. McAneney, 2007: Evaluation of the AR4 climate models' simulated daily maximum temperature, minimum temperature, and precipitation over Australia using probability density functions. *J. Climate,* **20,** 4356–4376.

——, ——, and S. Sisson, 2013: Systematic differences in future 20 year temperature extremes in AR4 model projections over Australia as a function of model skill. *Int. J. Climatol.,* **33,** 1153–1167.

Pugh, D., 1982: Estimating extreme currents by combining tidal and surge probabilities. *Ocean Eng.,* **9,** 361–372.

——, and J. Vassie, 1980: Application of the joint probability method for extreme sea level computations. *Proc. Inst. Civil Eng.,* **69,** 959–975.

Randall, D. A., and Coauthors, 2007: Climate models and their evaluation. *Climate Change 2007: The Physical Science Basis,* S. Solomon et al., Eds., Cambridge University Press, 589–662.

Ridgway, K. R., 2007: Long-term trend and decadal variability of the southward penetration of the East Australian Current. *Geophys. Res. Lett.,* **34,** L13613, doi:10.1029/2007GL030393.

Shane, R., and W. Lynn, 1964: Mathematical model for flood risk evaluation. *J. Hydraul. Eng.,* **90,** 1–20.

Simolo, C., M. Brunetti, M. Maugeri, and T. Nanni, 2011: Evolution of extreme temperatures in a warming climate. *Geophys. Res. Lett.,* **38,** L16701, doi:10.1029/2011GL048437.

Spiegelhalter, D., N. Best, B. Carlin, and A. Van Der Linde, 2002: Bayesian measures of model complexity and fit. *J. Roy. Stat. Soc.,* **64B,** 583–639.

Stammer, D., 1997: Global characteristics of ocean variability estimated from regional TOPEX/POSEIDON altimeter measurements. *J. Phys. Oceanogr.,* **27,** 1743–1769.

Sun, C., M. Feng, R. J. Matear, M. A. Chamberlain, P. Craig, K. R. Ridgway, and A. Schiller, 2012: Marine downscaling of a future climate scenario for Australian boundary currents. *J. Climate,* **25,** 2947–2962.

Suthers, I. M., and Coauthors, 2011: The strengthening East Australian Current, its eddies and biological effects—An introduction and overview. *Deep-Sea Res. II,* **58,** 538–546.

Tawn, J., 1992: Estimating probabilities of extreme sea-levels. *Appl. Stat.,* **41,** 77–93.

——, and J. Vassie, 1989: Extreme sea levels: The joint probability method revisited and revised. *Proc. Inst. Civil Eng.,* **87,** 429–442.

Thompson, K. R., and E. Demirov, 2006: Skewness of sea level variability of the world's oceans. *J. Geophys. Res.,* **111,** C05005, doi:10.1029/2004JC002839.

Todorovic, P., and E. Zelenhasic, 1970: A stochastic model for flood analysis. *Water Resour. Res.,* **6,** 1641–1648.

Uppala, S. M., and Coauthors, 2005: The ERA-40 Re-Analysis. *Quart. J. Roy. Meteor. Soc.,* **131,** 2961–3012.

Wernberg, T., D. A. Smale, F. Tuya, M. S. Thomsen, T. J. Langlois, T. de Bettignies, S. Bennett, and C. S. Rousseaux, 2012: An extreme climatic event alters marine ecosystem structure in a global biodiversity hotspot. *Nat. Climate Change,* **3,** 78–82.

Zwiers, F., 1987: An extreme-value analysis of wind speeds at five Canadian locations. *Can. J. Stat.,* **15,** 317–327.